Supplementary Information

High-voltage degradation mechanism of $NaNi_{1/3}Fe_{1/3}Mn_{1/3}O_2$ cathode in cycling pouch batteries

Shini Lin [a], Wei Li [a], Huiya Yang [a],Minghui Chen [a], Honghao Xie [a], Yuan Qin [a], Jing Zeng *[a], Peng Zhang *[b] and Jinbao Zhao *[a]

a. State-Province Joint Engineering Laboratory of Power Source Technology for New Energy Vehicle, State Key Laboratory of Physical Chemistry of Solid Surfaces, Engineering Research Center of Electrochemical Technology, Collaborative Innovation Center of Chemistry for Energy Materials, College of Chemistry and Chemical Engineering, Ministry of Education, Xiamen University, Xiamen 361005, China

b. College of Energy & School of Energy Research, Xiamen University, Xiamen 361102, China

† Electronic supplementary information (ESI) available. See DOI: 10.1039/x0xx00000x

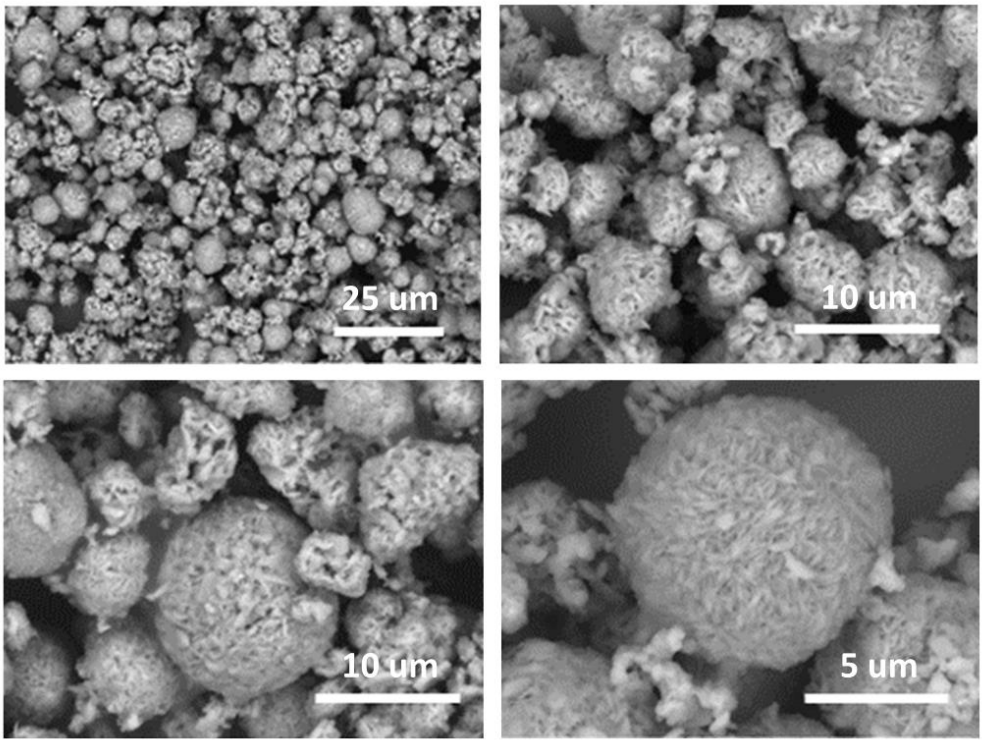

Fig. S1 SEM images of NFM.

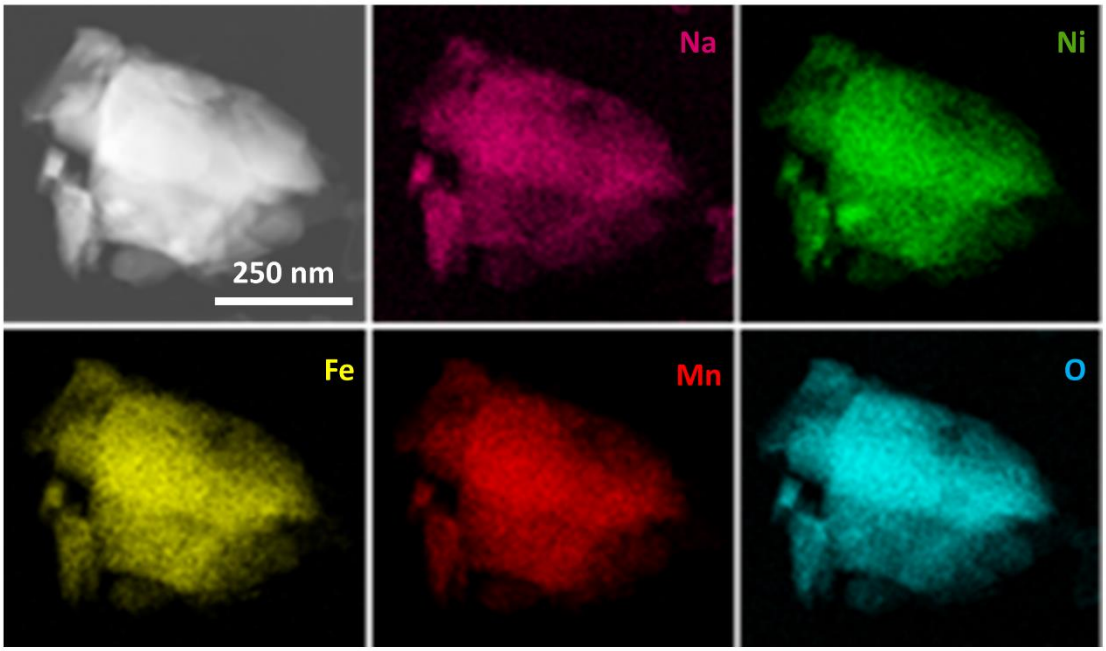

Fig. S2 TEM and elemental mapping images of NFM.

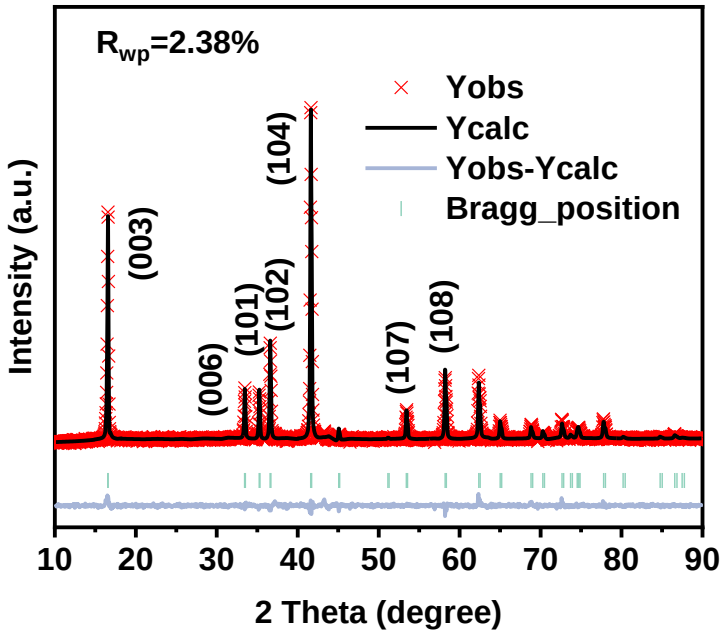

Fig. S3 XRD pattern of NFM. NFM has a hexagonal O3–$NaFeO_2$ structure with $R\bar{3}m$ space group, and the Bragg peak at 16.53° corresponds to the TMO_6 slabs ($d_{(003)}$) with 0.536 nm spacing which indicates the size of Na^+ transport channel.

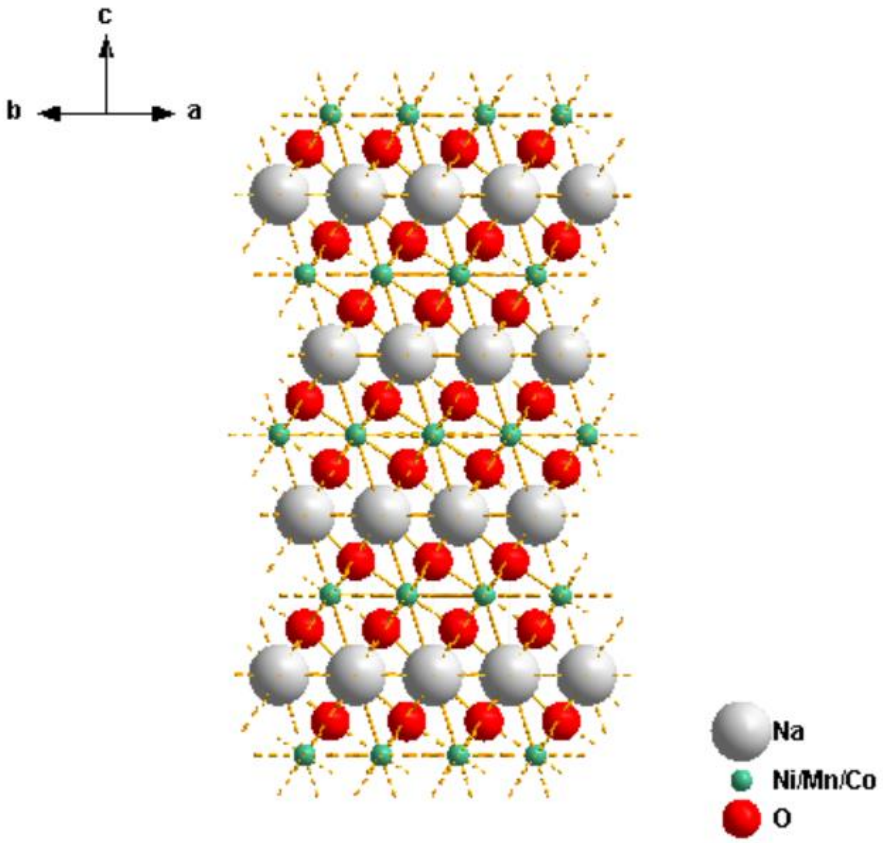

Fig. S4 Structure model of NFM.

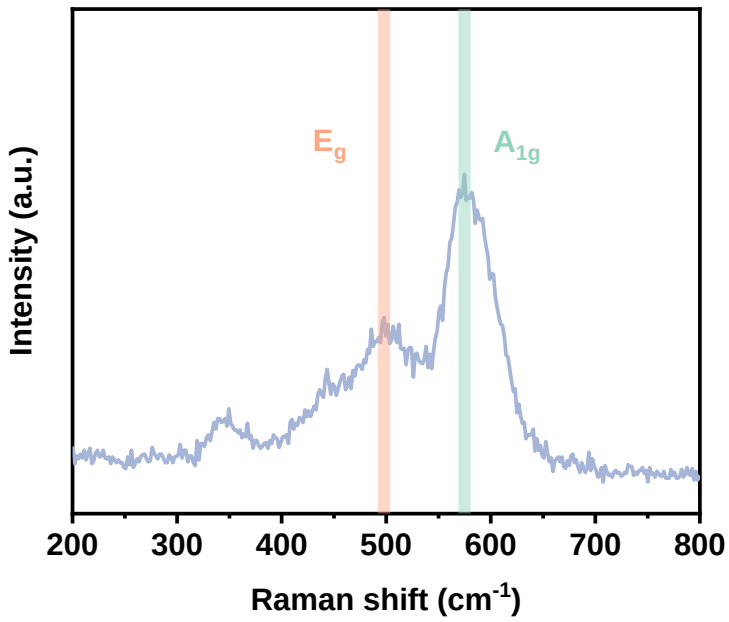

Fig. S5 Raman spectrum of NFM. The two Raman peaks at 498 cm^{-1} (E_g) and 575 cm^{-1} (A_{1g}) correspond to the bending vibration and stretching vibration of TM-O bonds respectively.

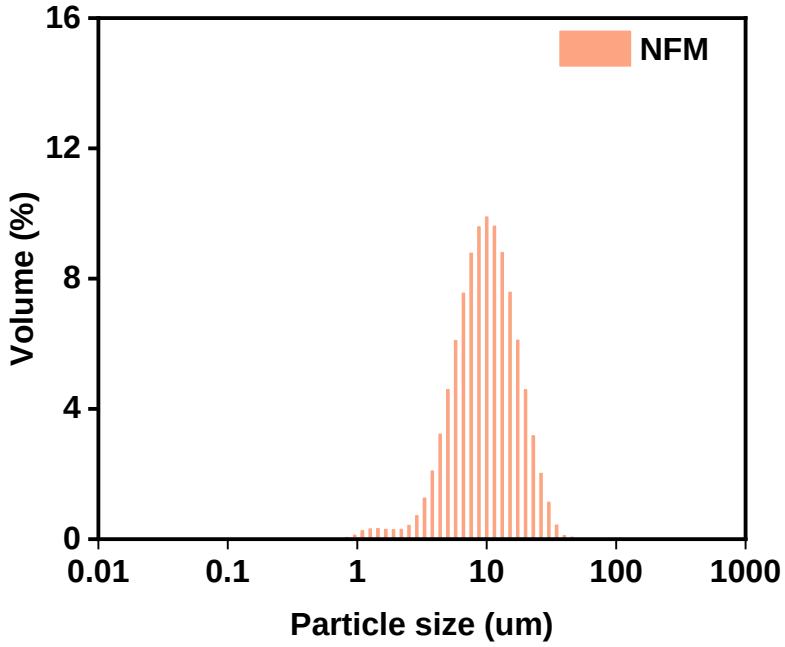

Fig. S6 Particle-size distribution of NFM through laser analysis (D_{50}=10.2 μm).

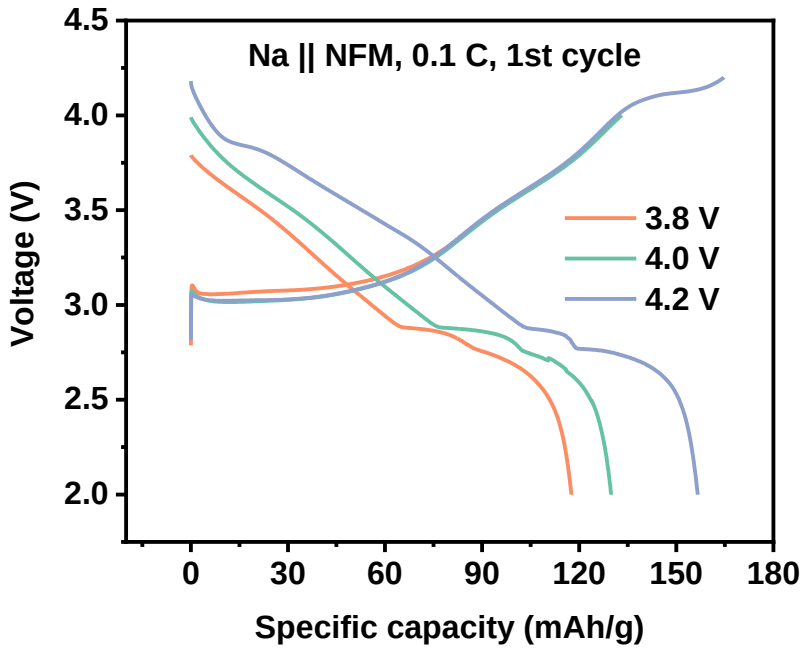

Fig. S7 Galvanostatic charge/discharge curves of NFM at 0.1 C of the 1st cycle with 3.8 V, 4.0 V and 4.2 V upper voltages.

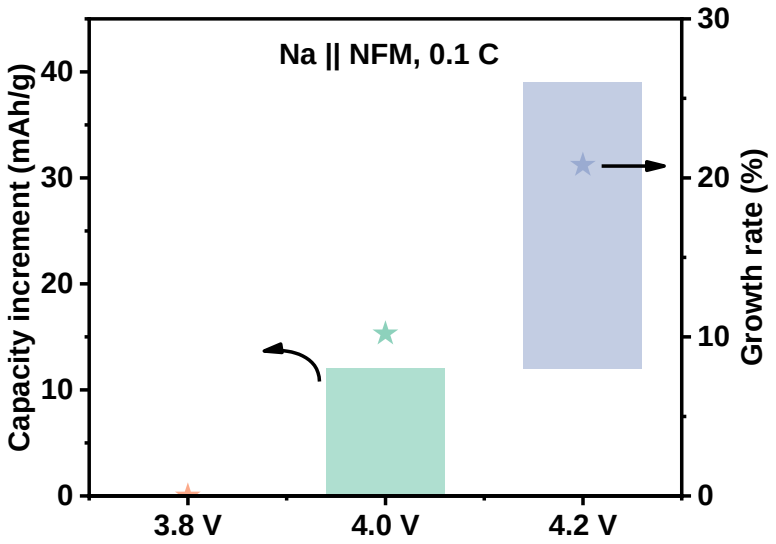

Fig. S8 Capacity increment with the charging cut-off voltage increse of NFM. When the charging cut-off voltage increases from 4.0 V to 4.2 V, the high voltage plateau located at 4.12 V (charge)/3.85 V (discharge) appears contributing to the significant capacity increment, and the discharge voltage significantly rises, indicating the large energy increment at 4.2 V.

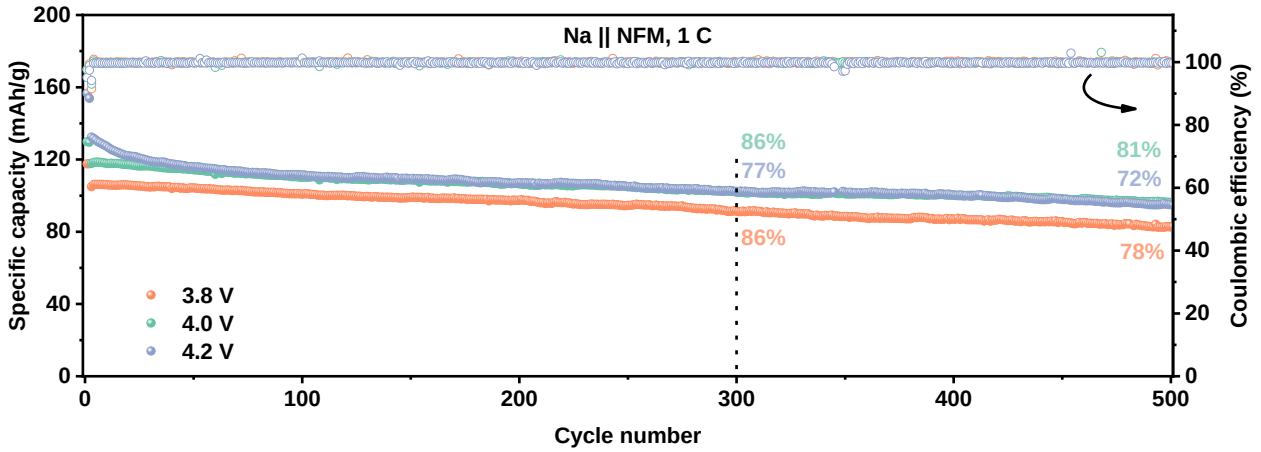

Fig. S9 Cycling performance of NFM at different charging cut-off voltage. At 4.0 V upper voltage, NFM shows the best balance between high capacity and long cycle life.

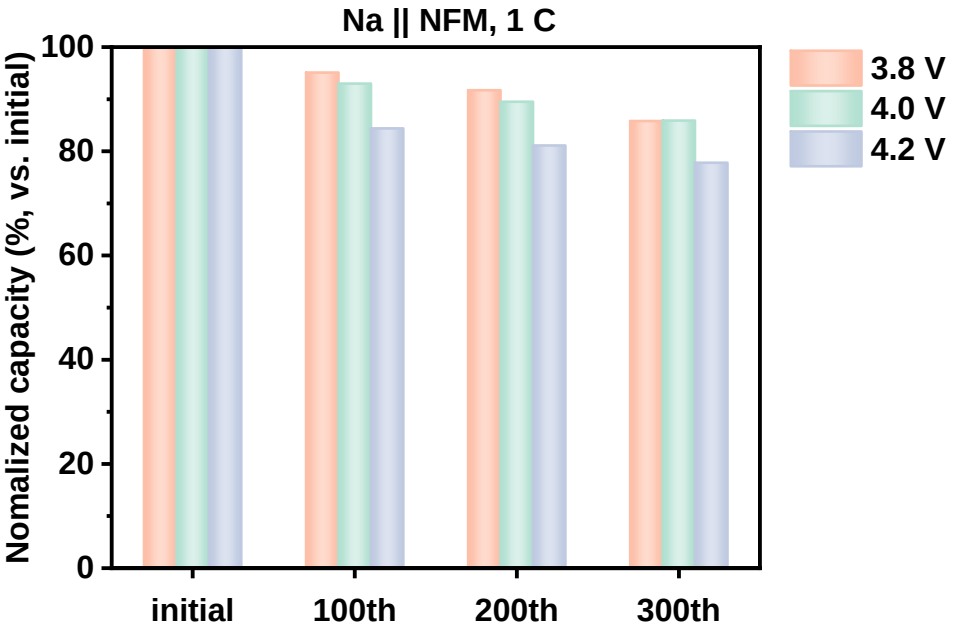

Fig. S10 Remaining capacity ratio with the cycling for NFM at different charging cut-off voltage.

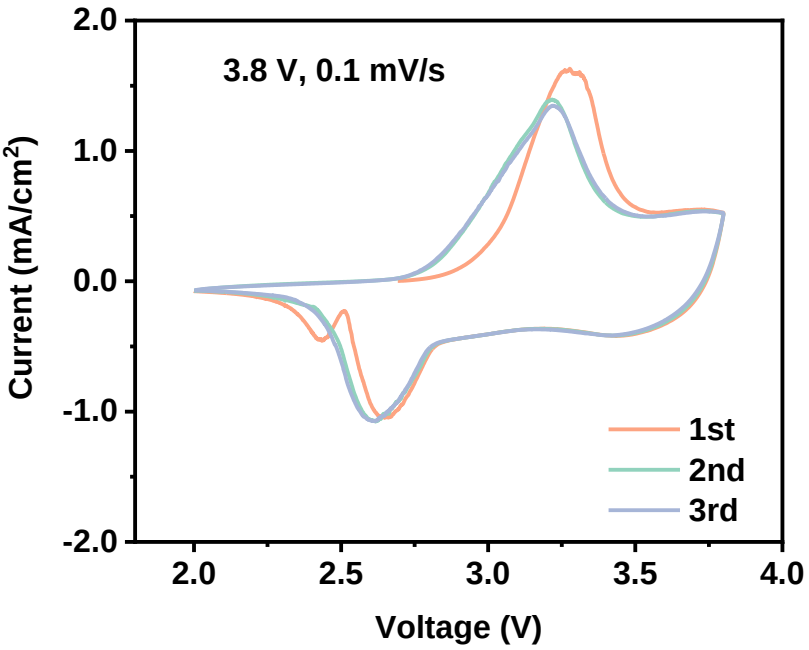

Fig. S11 Cyclic voltammetry of NFM at 3.8 V cut-off voltage for 3 cycles.

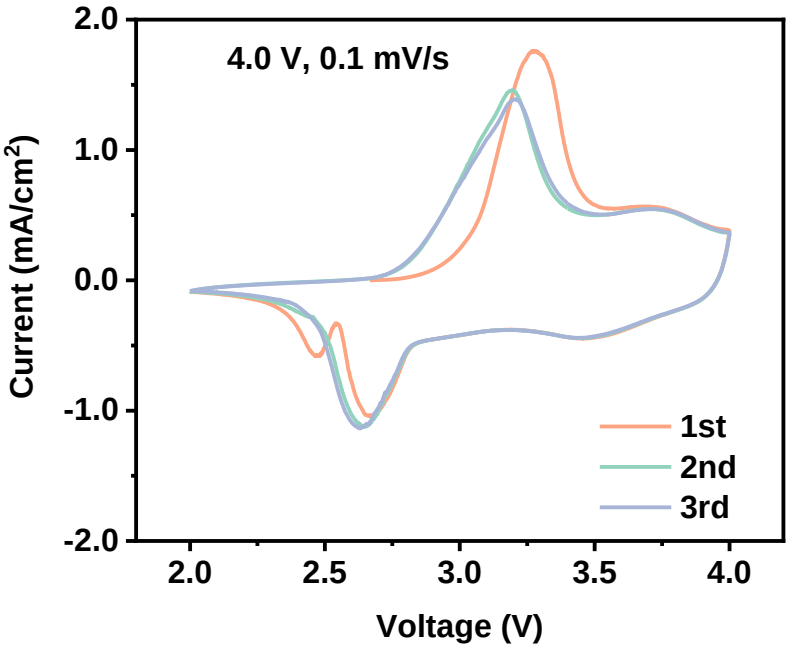

Fig. S12 Cyclic voltammetry of NFM at 4.0 V cut-off voltage for 3 cycles.

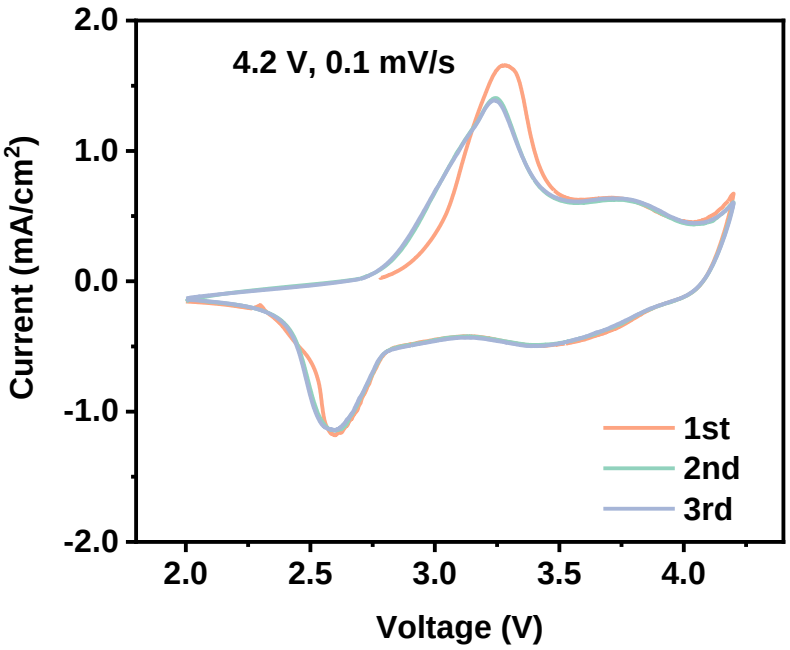

Fig. S13 Cyclic voltammetry of NFM at 4.2 V cut-off voltage for 3 cycles.

CV results show two pairs of redox peaks at 3.28/2.64 V and 3.73/3.46 V attributed to the Ni^{2+}/Ni^{4+} and Fe^{3+}/Fe^{4+} redox couples respectively[1], well matching the voltage plateau of galvanostatic charge/discharge curves. Notably, the oxidation peak near 4.2 V in Fig. S13 indicates the Fe^{3+}/Fe^{4+}

redox reaction. When the charging cut-off voltage is under 4.0 V, the charge compensation is dominant by Ni^{2+}/Ni^{4+} via Ni^{3+} redox reaction. While for the charging voltage above 4.0 V, it is mainly dominant by Fe^{3+}/Fe^{4+} with slight Ni^{2+}/Ni^{4+}. The Fe^{3+}/Fe^{4+} redox reaction is accompanied with Jahn-Teller Fe^{4+} and Fe migration from TM slabs to Na slabs, causing the structural distortion and the harmful X and O3' phases shown in Fig. 3d.

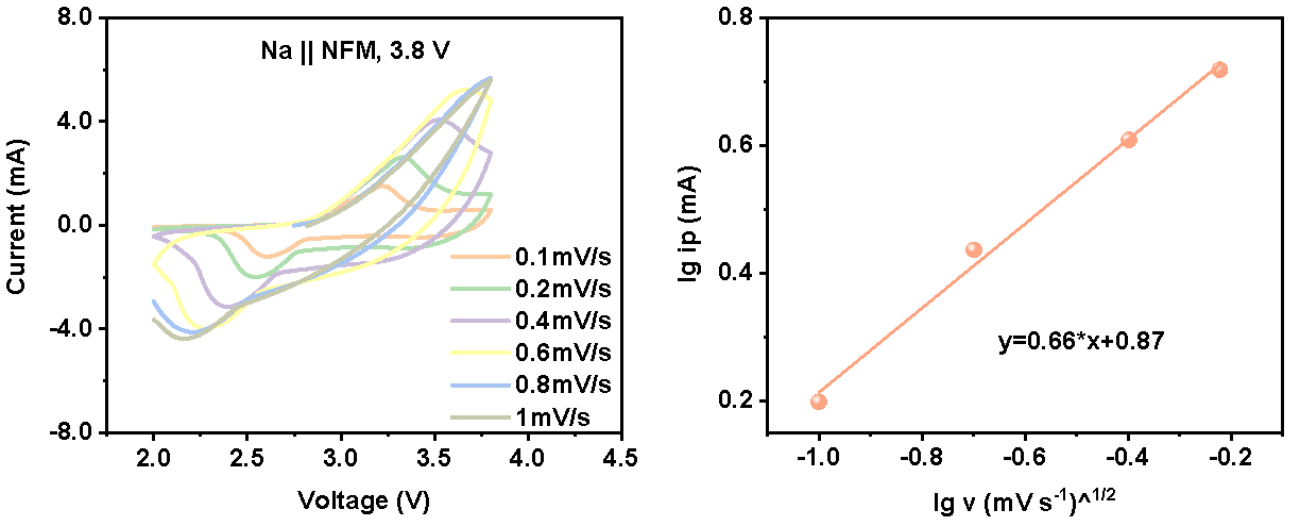

Fig. S14 (a) Variable scan-rate CV curves and (b) linear fitting of lg i_p ~ lg v according to the oxidation peaks of initial NFM at 3.8 V cut-off voltage.

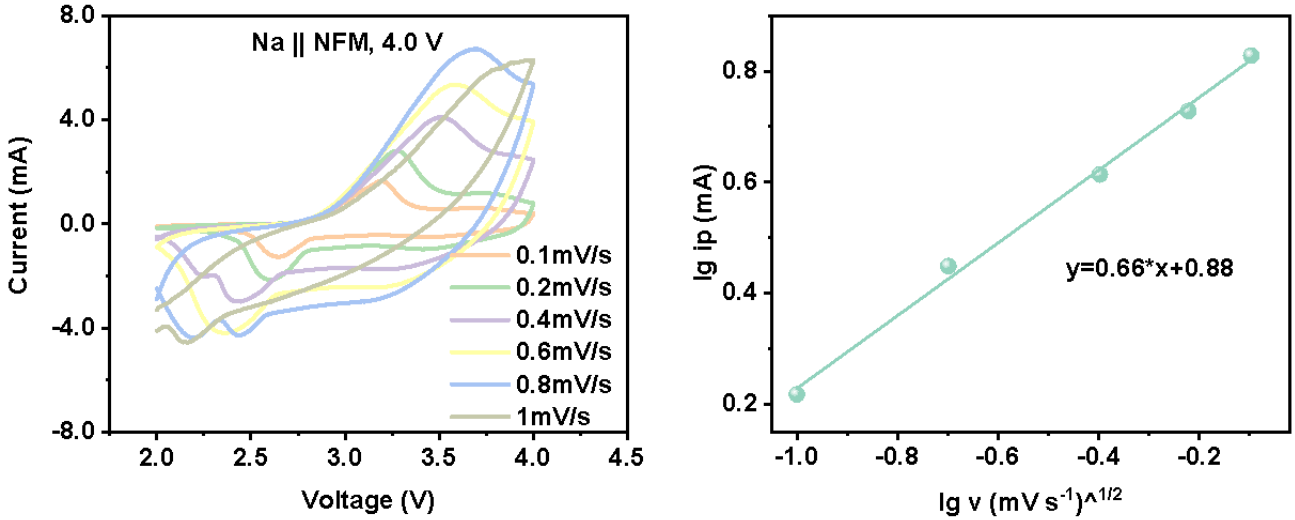

Fig. S15 (a) Variable scan-rate CV curves and (b) linear fitting of lg i_p ~ lg v according to the oxidation peaks of initial NFM at 4.0 V cut-off voltage.

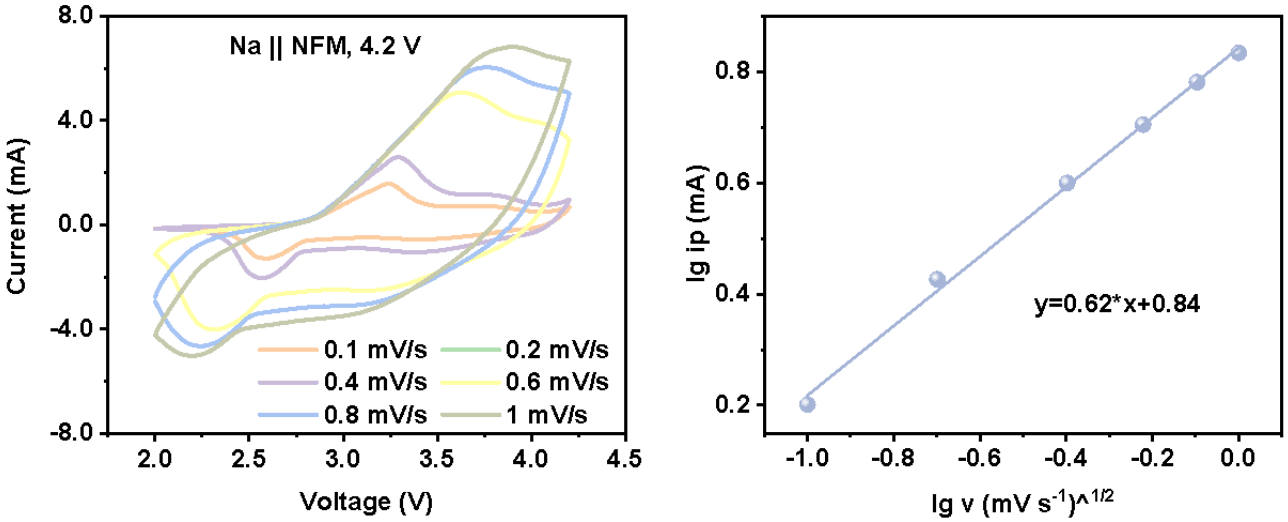

Fig. S16 (a) Variable scan-rate CV curves and (b) linear fitting of lg i_p ~ lg v according to the oxidation peaks of initial NFM at 4.2 V cut-off voltage.

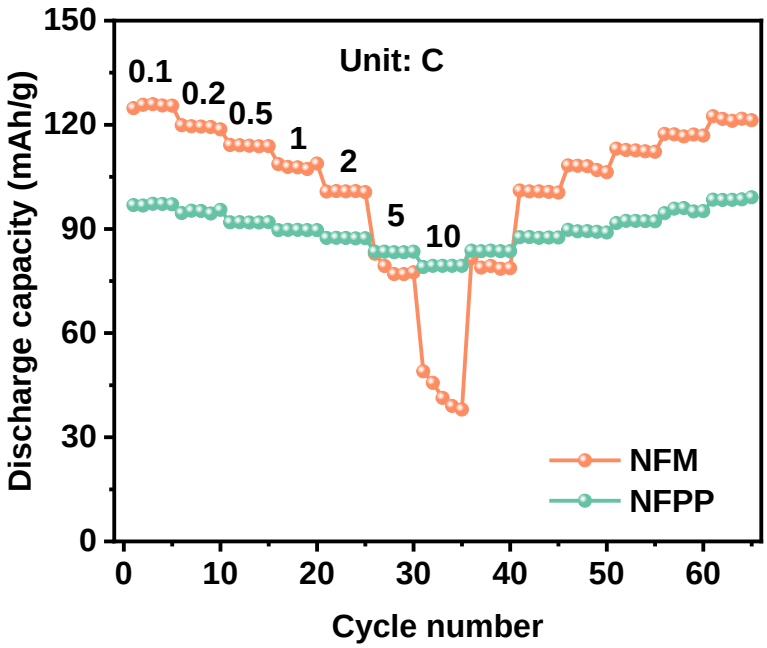

Fig. S17 Rate performance of NFM (NFPP as the reference object).

According to formula 1, the reactions in NFM cathode is mainly Na^+ diffusion-controlled and slightly capacitive-controlled which indicates the sluggish kinetics in NFM and results in poor rate performance (Fig. S14-17). Additionally, the Na^+ diffusion behavior in NFM is independent of the increased charging cut-off voltage with the similar k.

$$i_p = k \times v^b$$

b=0.5, diffusion-controlled;

b=1, capacitive-controlled;

b=0.5~1, both controlled. 1

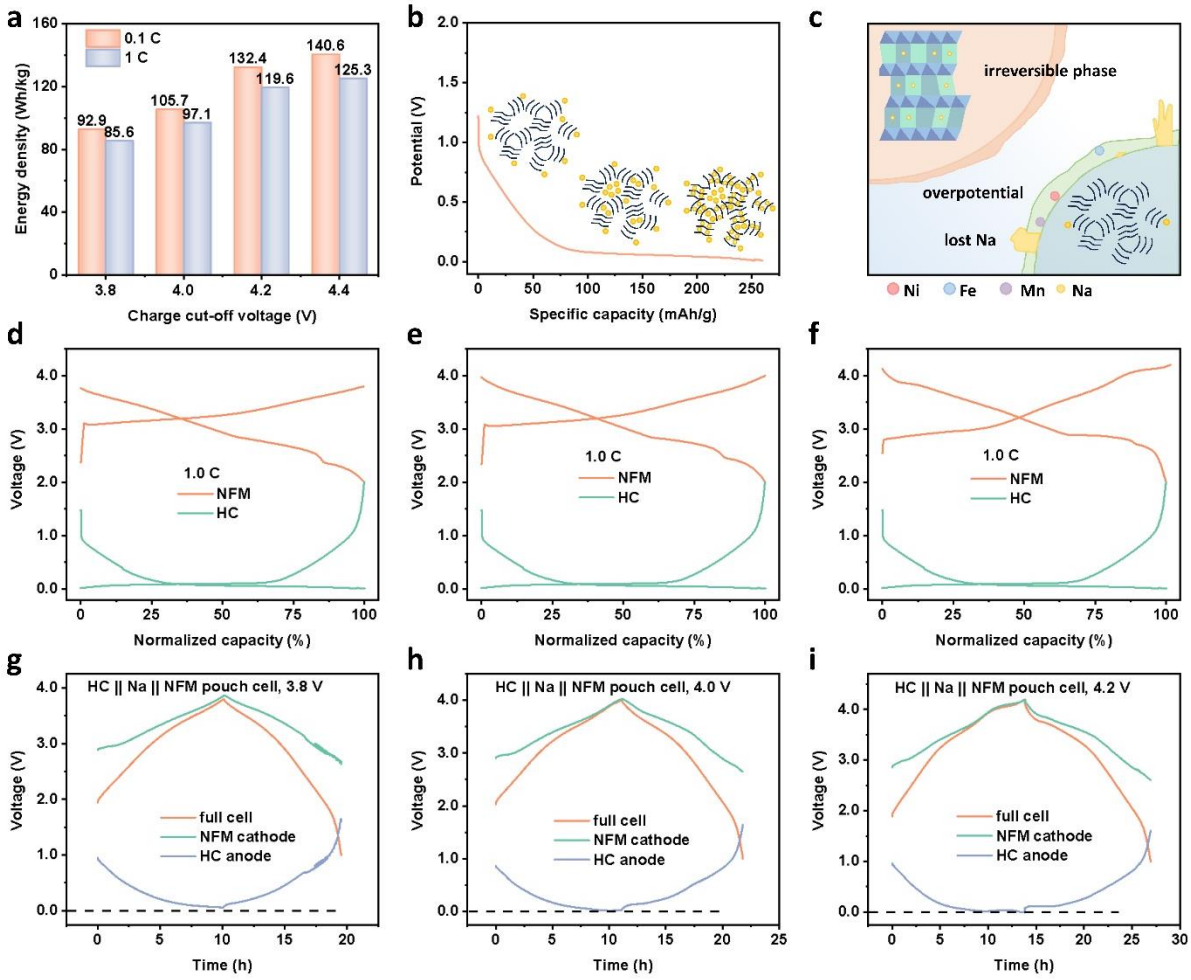

Fig. S18 (a) Energy density increase with charging cut-off voltage increase of HC||NFM pouch battery. (b) Sodium storage mechanism of HC. (c) Structural transition of NFM cathode due to the Na loss on HC anode. (d-f) Normalized-capacity charge/discharge curves of NFM and HC with the upper voltage of NFM at 3.8 V, 4.0 V and 4.2 V respectively. (g-i) Potential change of NFM cathode, HC anode and full battery during charge and discharge through three-electrode pouch battery measurements, with 3.8 V, 4.0 V, and 4.2 V upper voltages respectively.

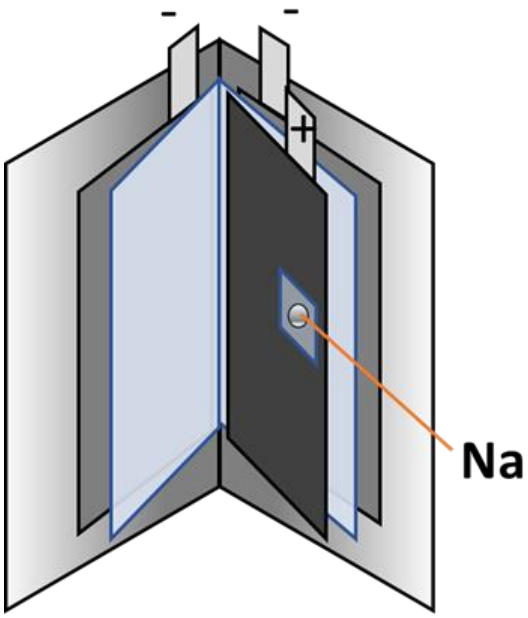

Fig. S19 Schematic diagram of three-electrode pouch cell (HC||Na||NFM).

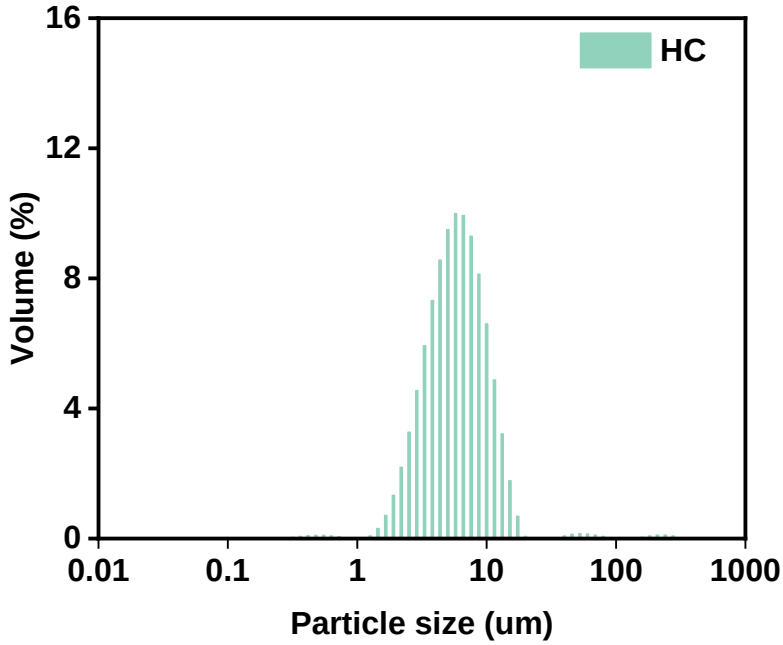

Fig. S20 Particle-size distribution of HC through laser analysis (D_{50}=5.4 μm).

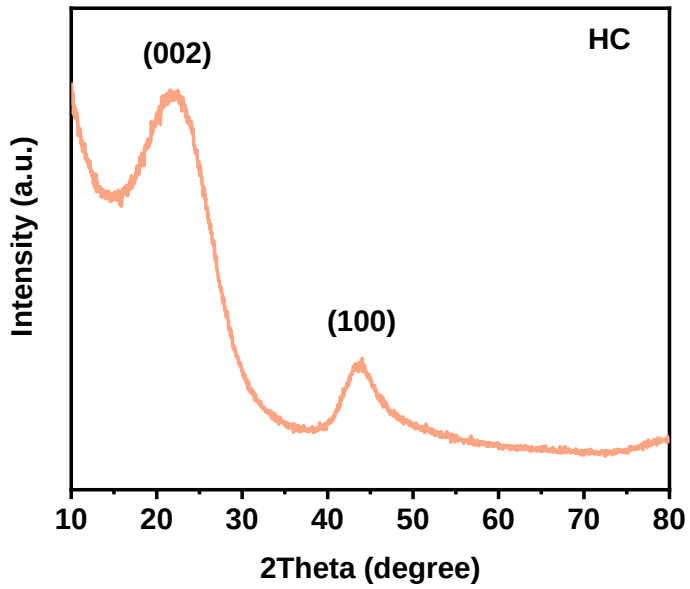

Fig. S21 XRD pattern of HC (the two broad peaks at 22.2° (3.729 Å, spacing of carbon lamellas) and 43.9° correspond to the (002) and (100) lattice planes respectively and indicate the disordered amorphous carbon structure of HC [2]).

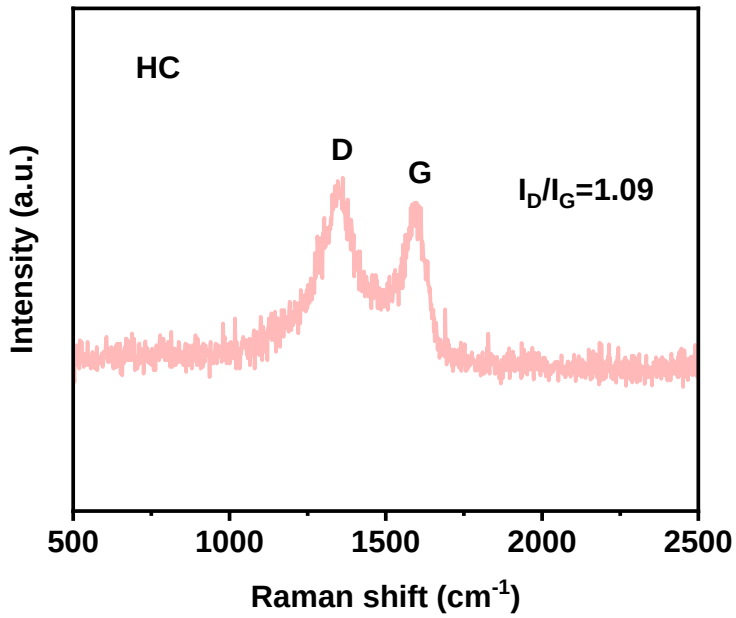

Fig. S22 Raman spectrum of HC (D band (1350 cm^{-1}) represents the A_{1g} mode of sp^2 carbon induced by respiratory vibration in disordered or defective carbon, and G band (1580 cm^{-1}) corresponds to the E_{2g} mode of vibration ascribed to sp^2 carbon in graphite rings or chains [3,4]).

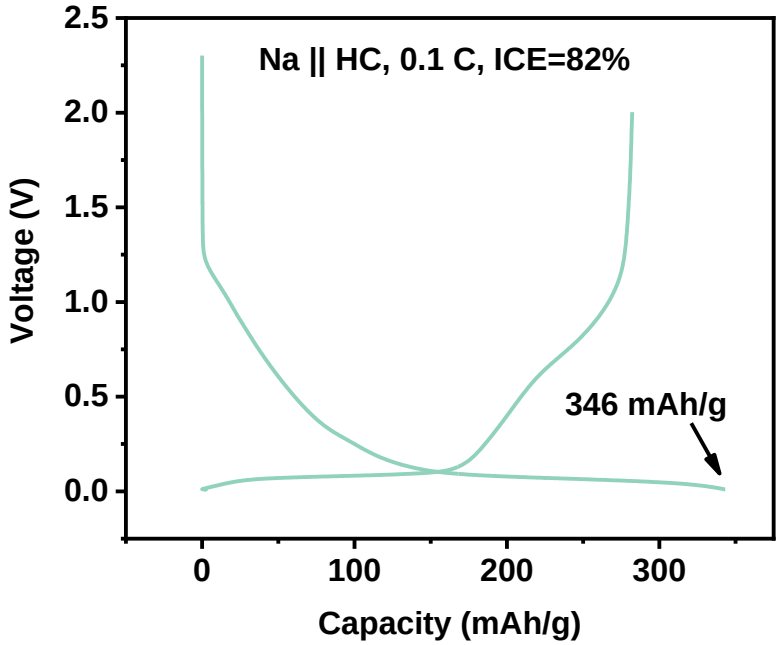

Fig. S23 Galvanostatic charge/discharge curves of HC in the 1st cycle at 0.1 C (157.6 mAh/g in slope region (45.6%) and 188.2 mAh/g in plateau region (54.4%), and 81.6% initial coulombic efficiency (ICE) indicating the certain loss of Na^+ to form SEI).

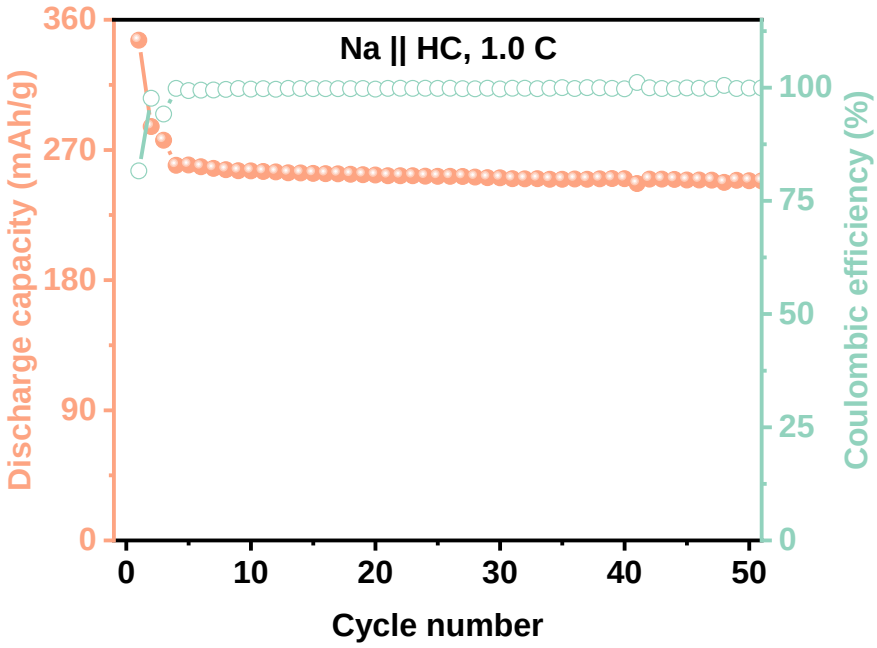

Fig. S24 Cycling performance of HC at 1 C (96.1% capacity retention after 50 cycles due to SEI dissolution and regeneration).

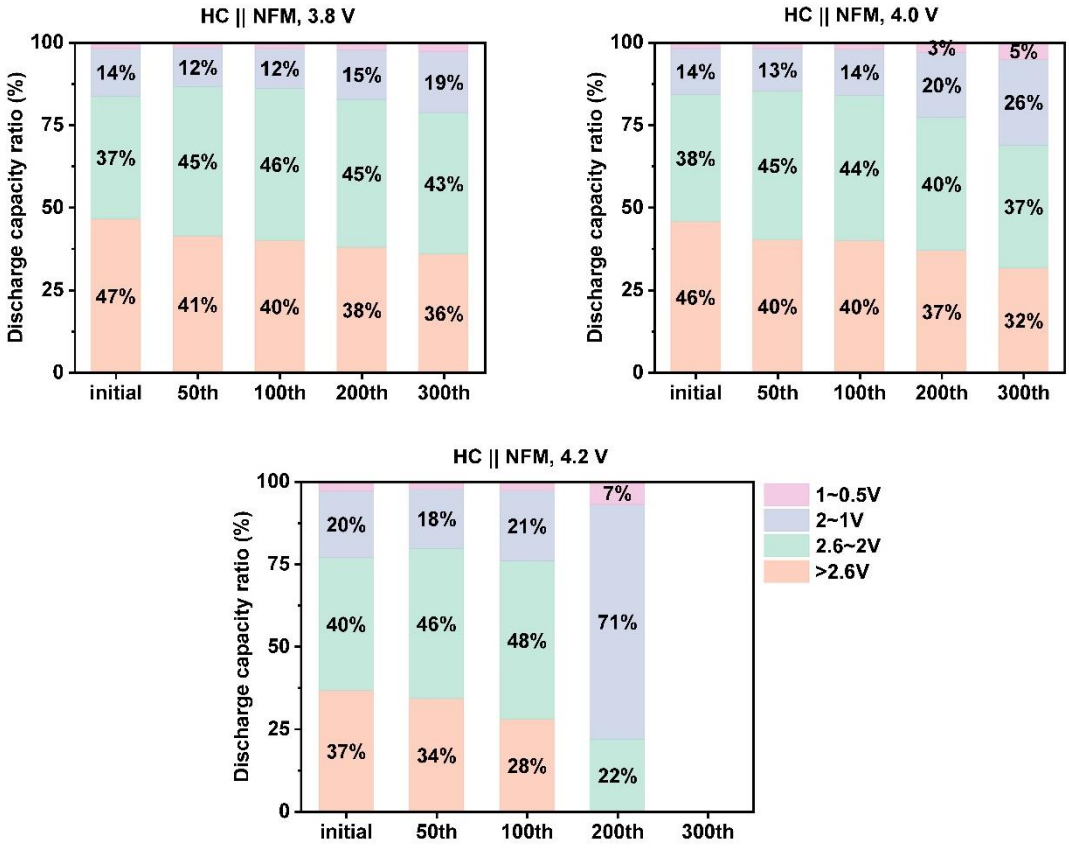

Fig. S25 Capacity distribution versus voltage of HC||NFM full cell at selected cycles at 3.8 V, 4.0 V and 4.2 V upper voltage.

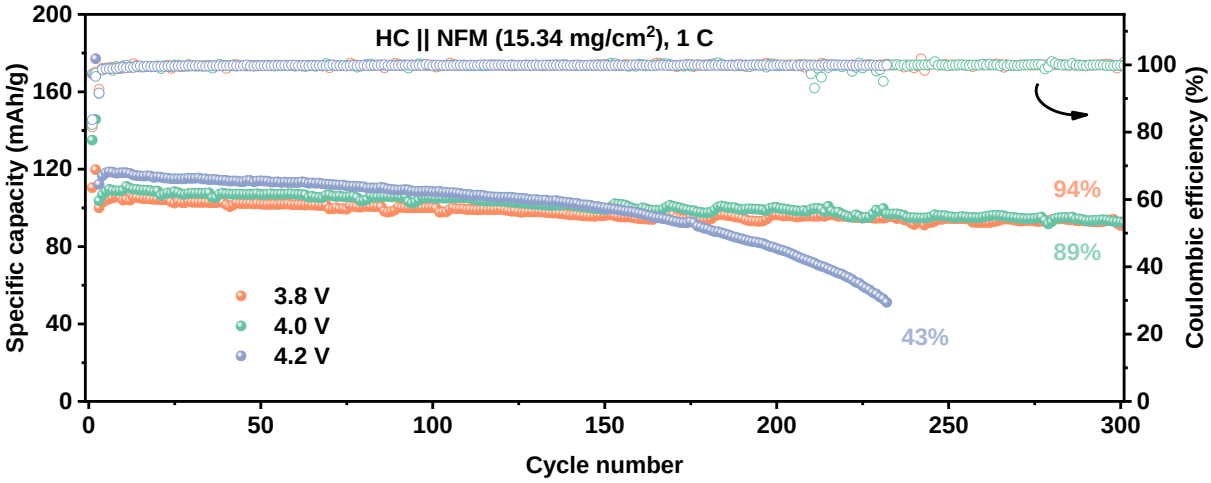

Fig. S26 Cycling performance of HC||NFM full cell at 3.8 V, 4.0 V and 4.2 V upper voltage.

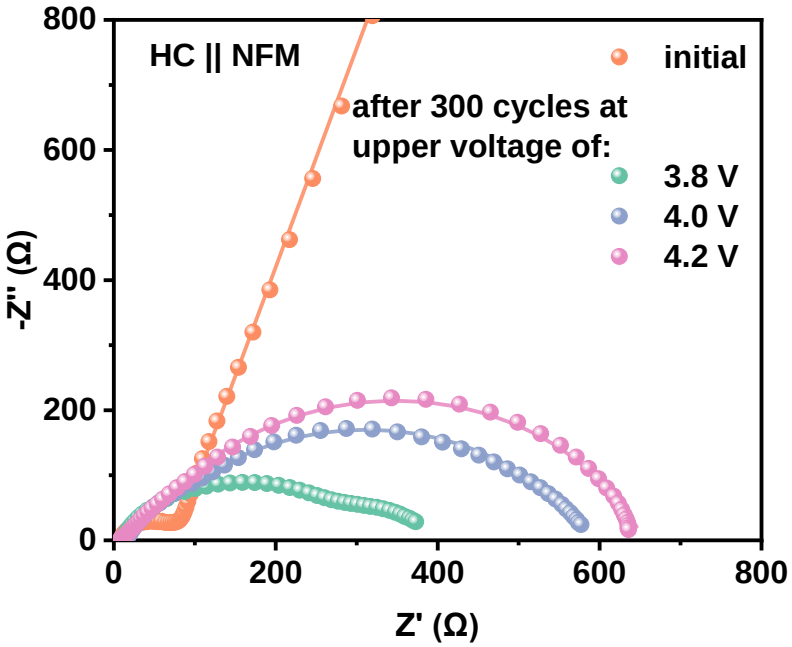

Fig. S27 EIS results of fresh and cycled HC||NFM cells.

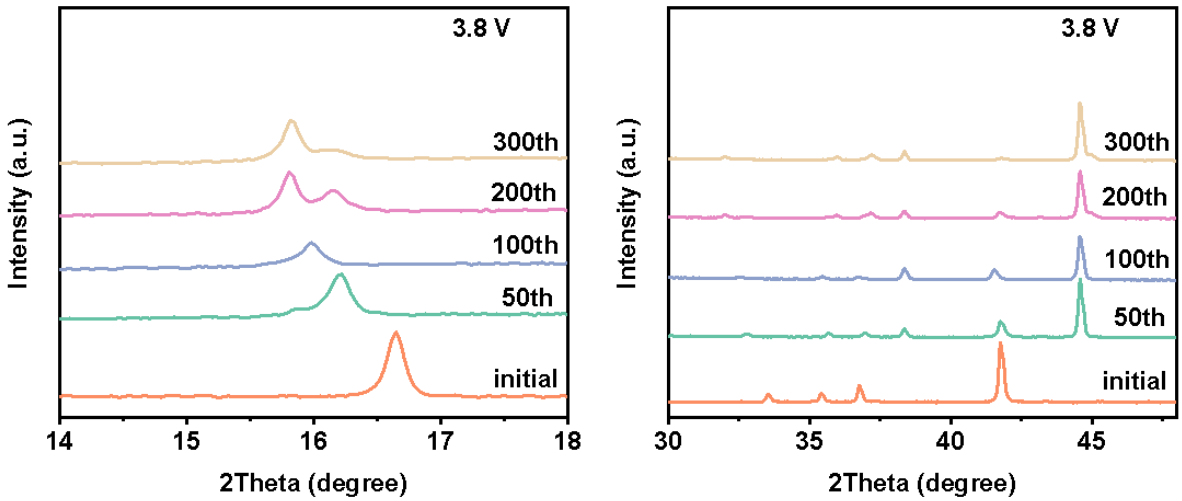

Fig. S28 Local post-mortem XRD patterns of NFM cathode from pouch cell cycling at 3.8 V.

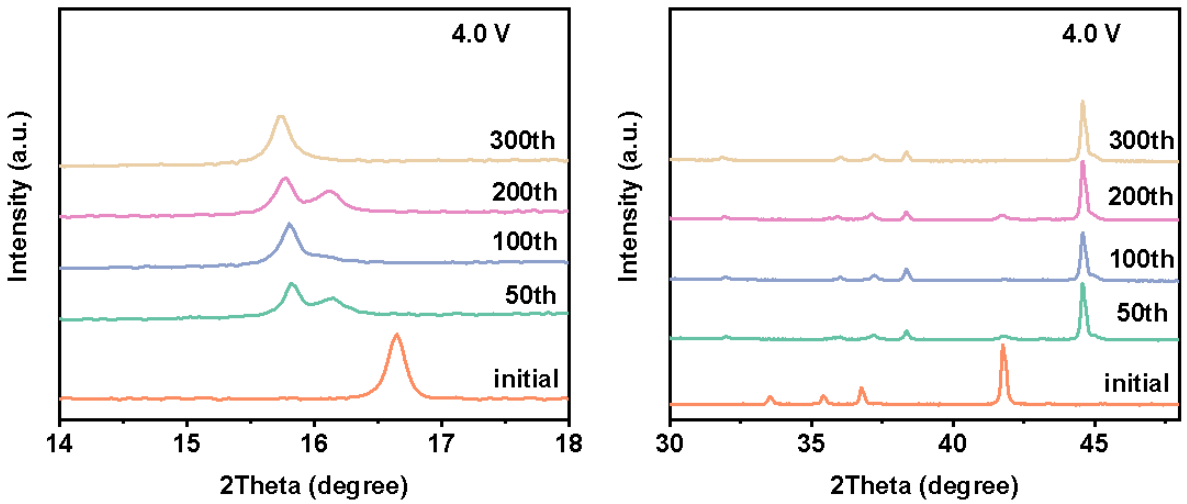

Fig. S29 Local post-mortem XRD patterns of NFM cathode from pouch cell cycling at 4.0 V.

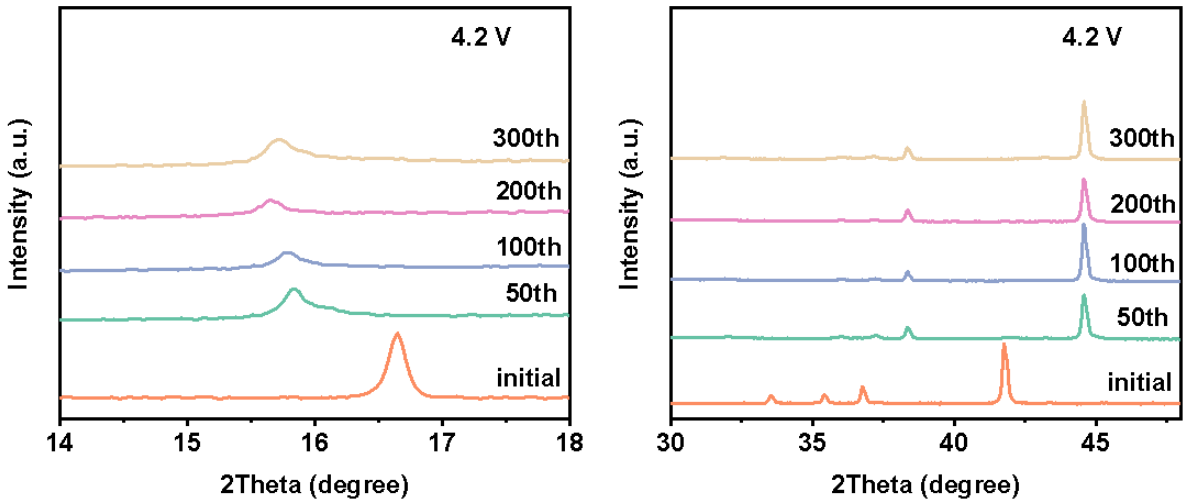

Fig. S30 Local post-mortem XRD patterns of NFM cathode from pouch cell cycling at 4.2 V.

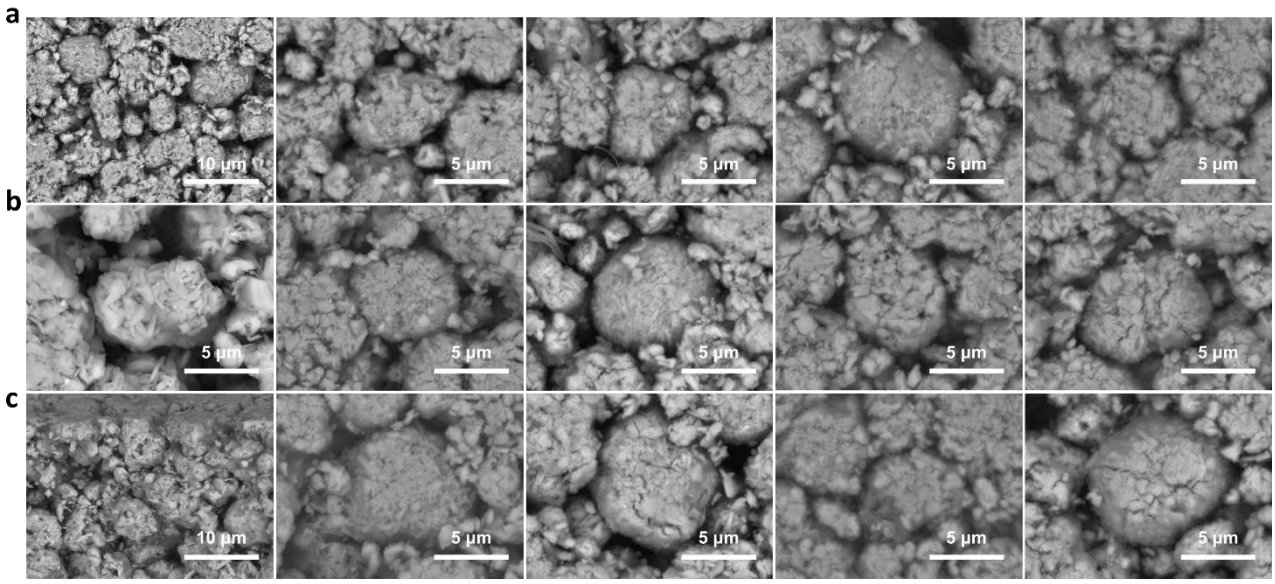

Fig. S31 SEM images of NFM cathode cycling in full batteries at 3.8 V (a), 4.0 V (b) and 4.2 V (c). Each column from left to right is the initial, the 50th cycle, the 100th cycle, the 200th cycle, and the 300th cycle.

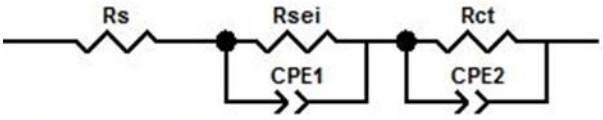

Fig. S32 Equivalent circuit model of NFM cathode.

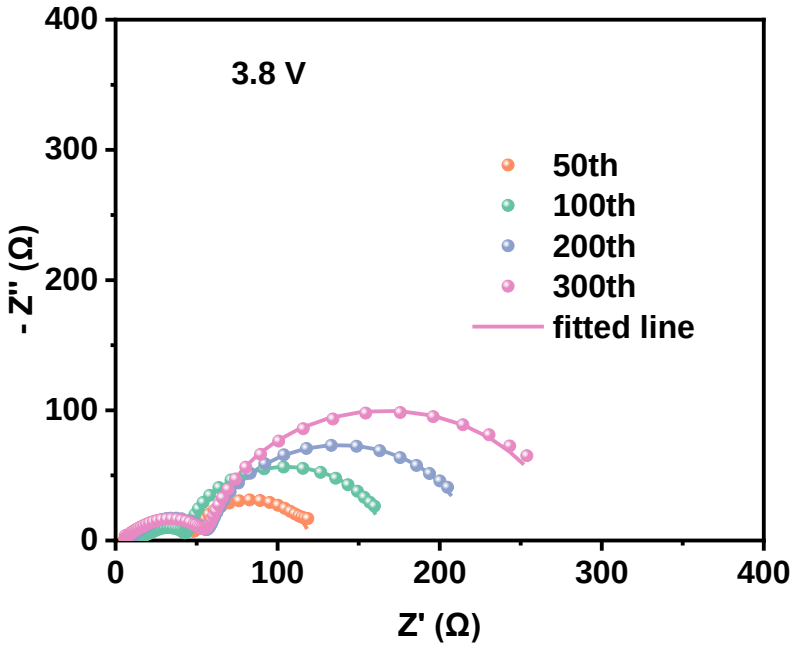

Fig. S33 EIS of Na||NFM with cycling at 3.8 V upper voltage.

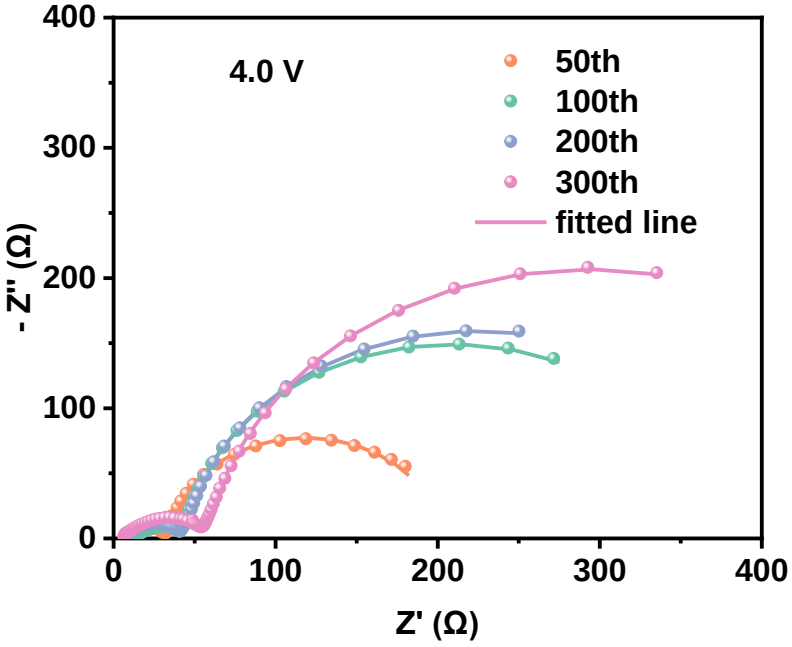

Fig. S34 EIS of Na||NFM with cycling at 4.0 V upper voltage.

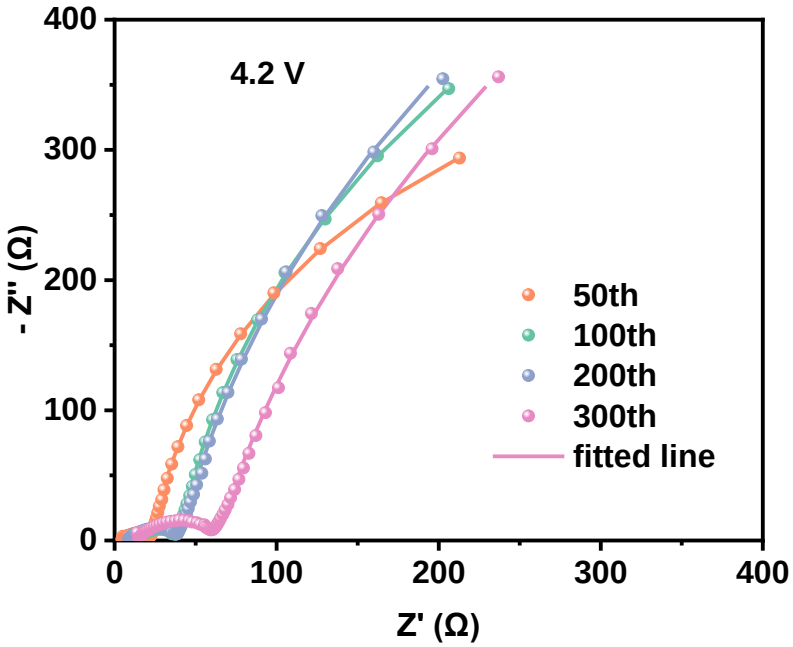

Fig. S35 EIS of Na||NFM with cycling at 4.2 V upper voltage.

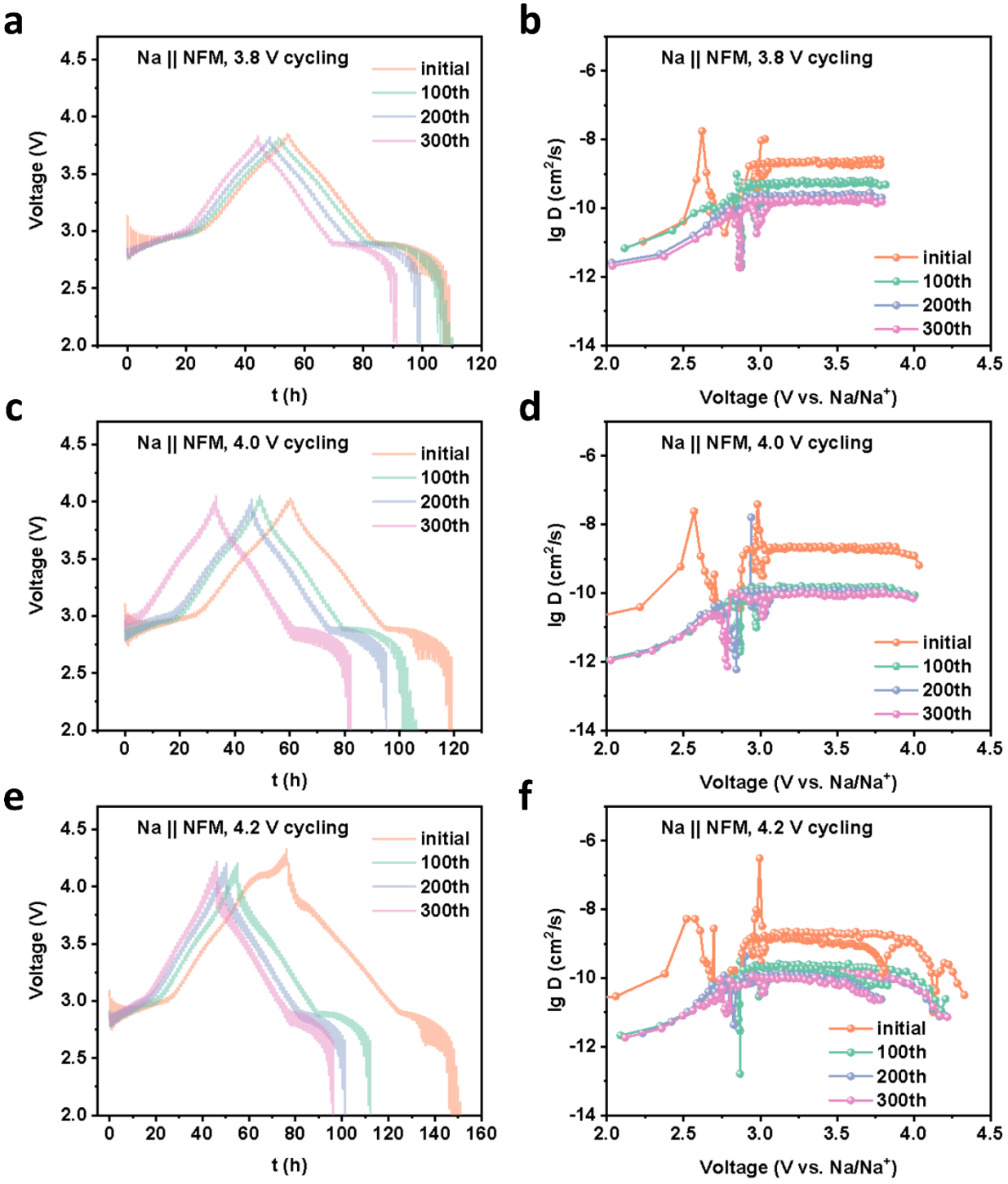

Fig. S36 GITT and D_{Na+} curves of NFM cathode cycling at (a, b) 3.8 V, (c, d) 4.0 V, and (e, f) 4.2 V upper voltages.

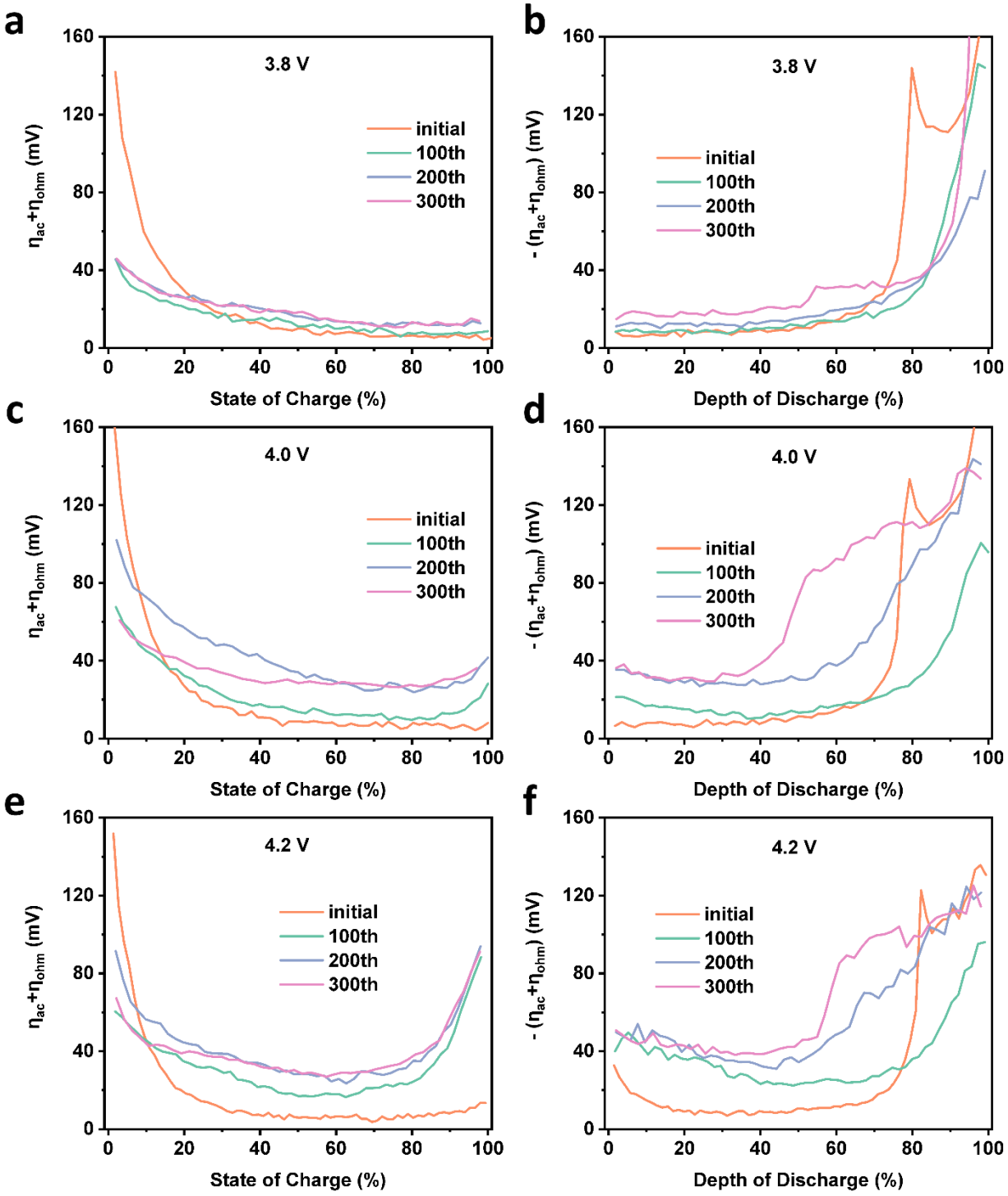

Fig. S37 Activation polarization + ohmic polarization cycling at (a, b) 3.8 V, (c, d) 4.0 V and (e, f) 4.2 V upper voltages.

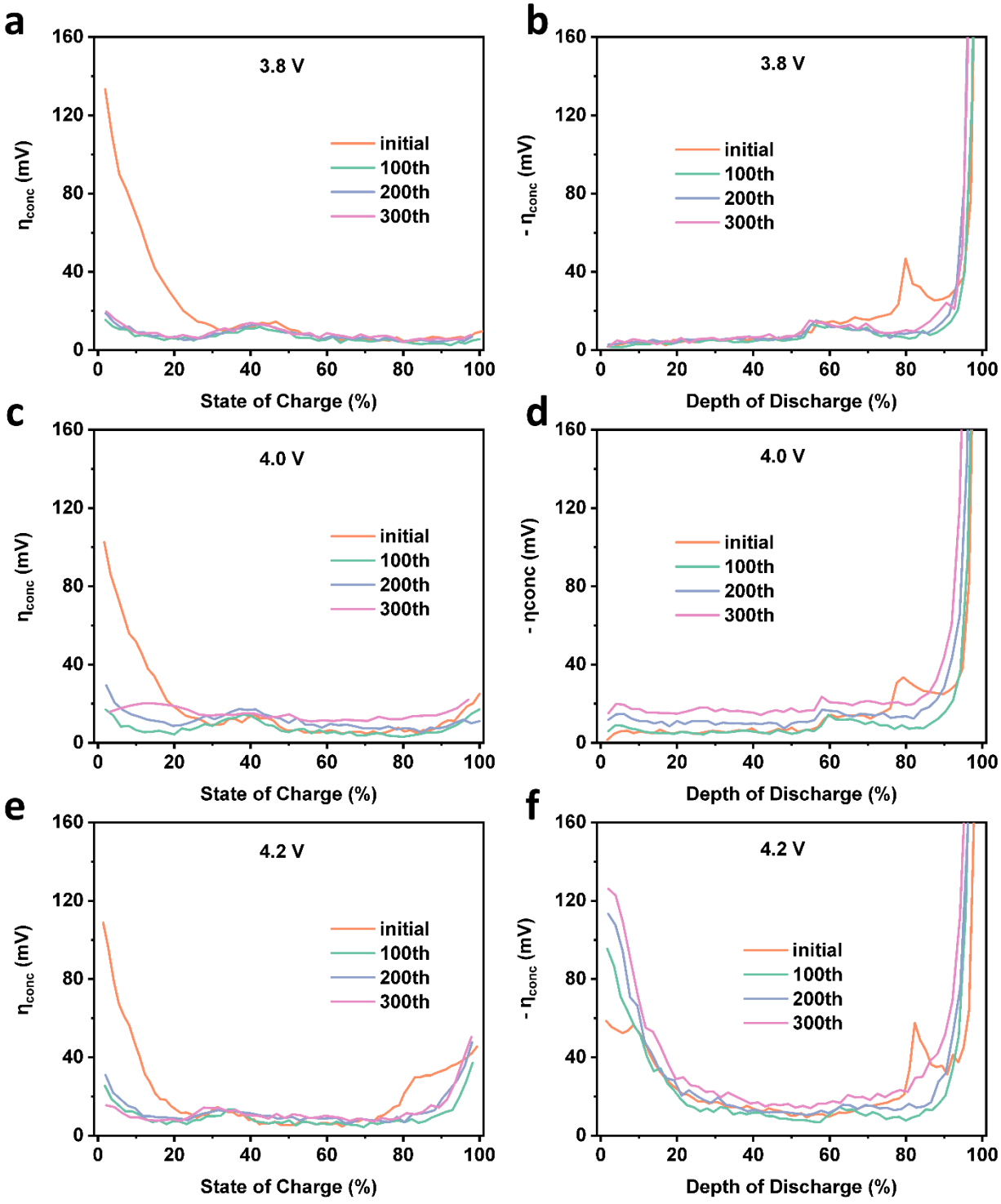

Fig. S38 Concentration polarization with cycling at (a, b) 3.8 V, (c, d) 4.0 V and (e, f) 4.2 V upper voltages.

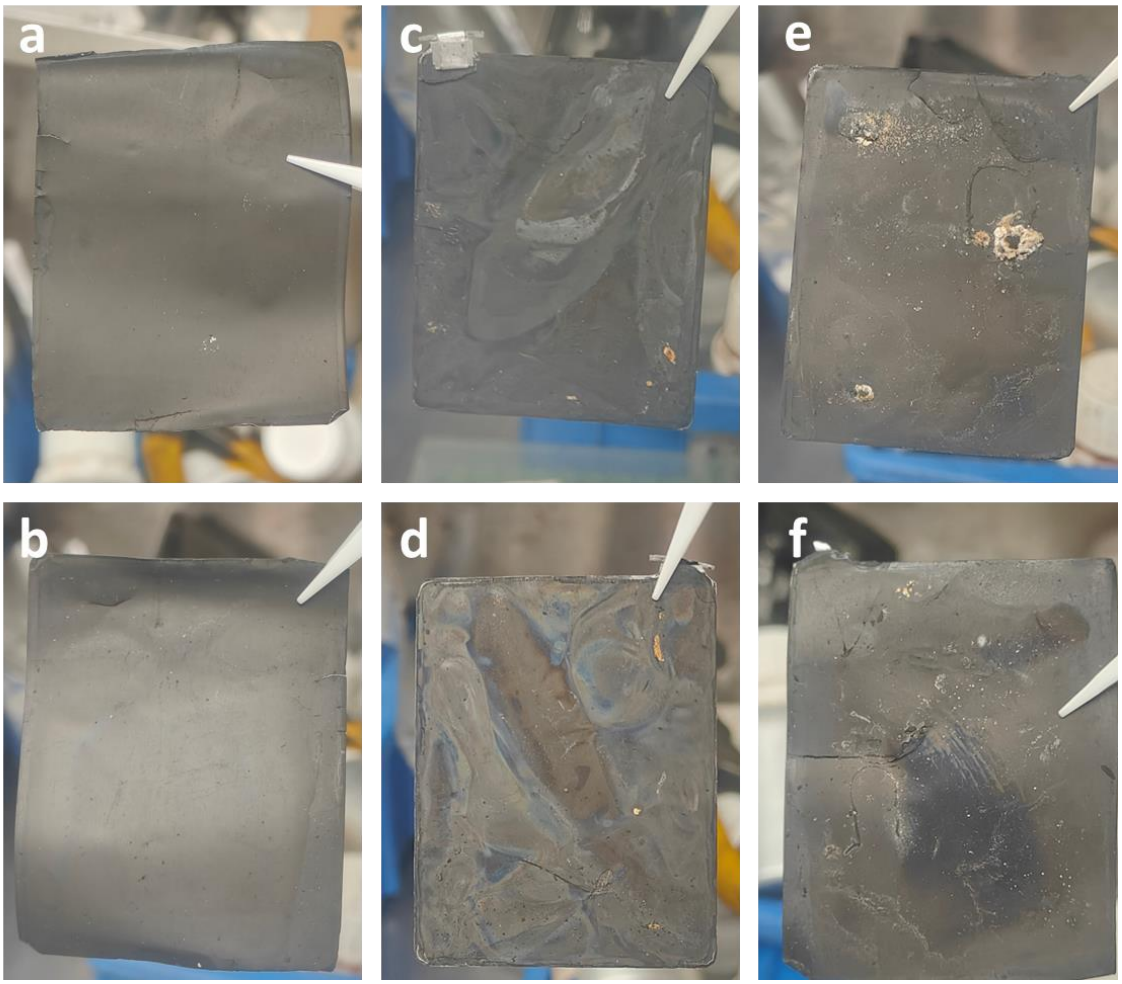

Fig. S39 Optical images of HC anode from HC||NFM pouch cells after 300 cycles under (a-b) 3.8 V, (c-d) 4.0 V, and (e-f) 4.2 V charging cut-off voltages.

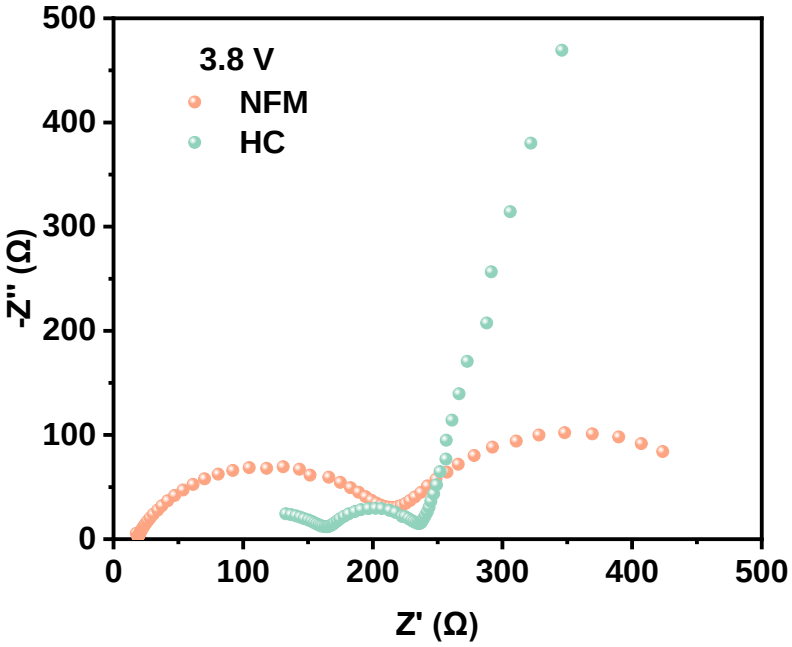

Fig. S40 EIS results of Na||NFM and Na||HC half cells (the NFM and HC electrodes were from the pouch cell after cycling at 3.8 V upper voltage).

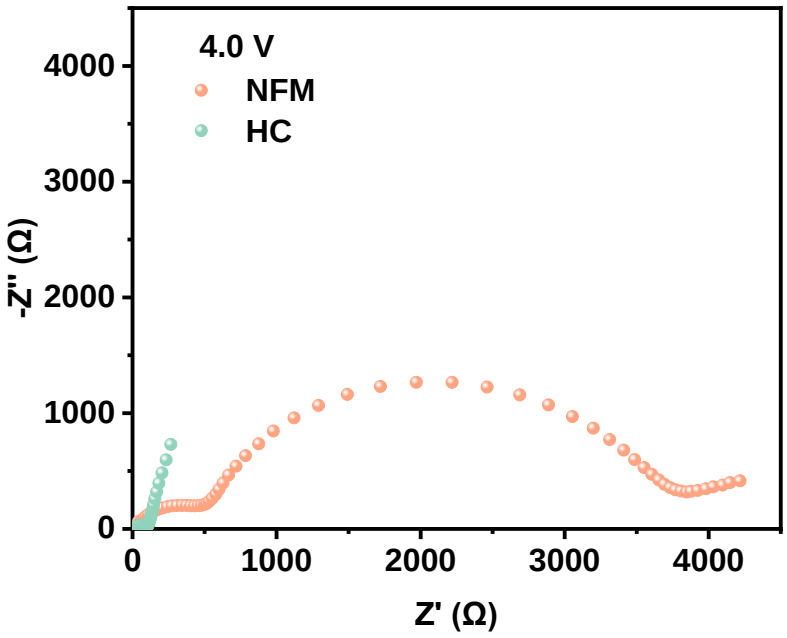

Fig. S41 EIS results of Na||NFM and Na||HC half cells (the NFM and HC electrodes were from the pouch cell after cycling at 4.0 V upper voltage).

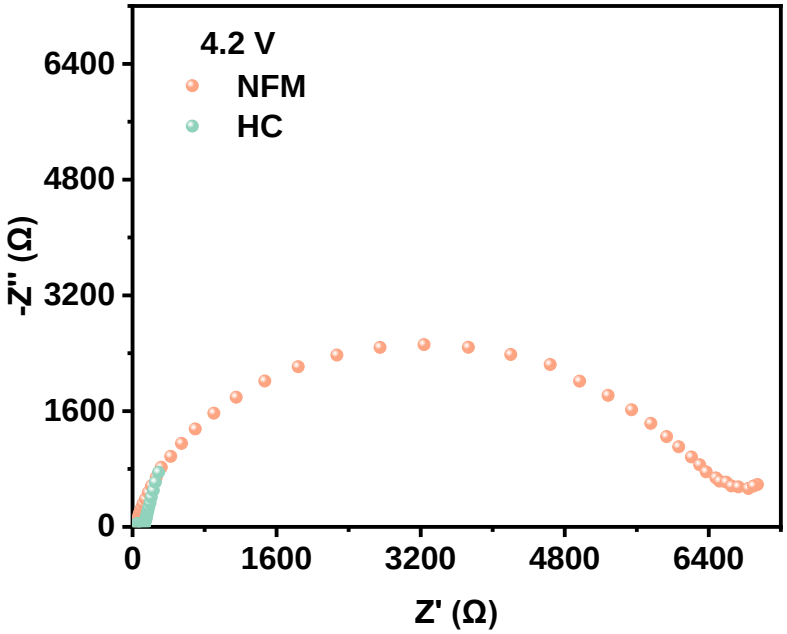

Fig. S42 EIS results of Na||NFM and Na||HC half cells (the NFM and HC electrodes were from the pouch cell after cycling at 4.2 V upper voltage).

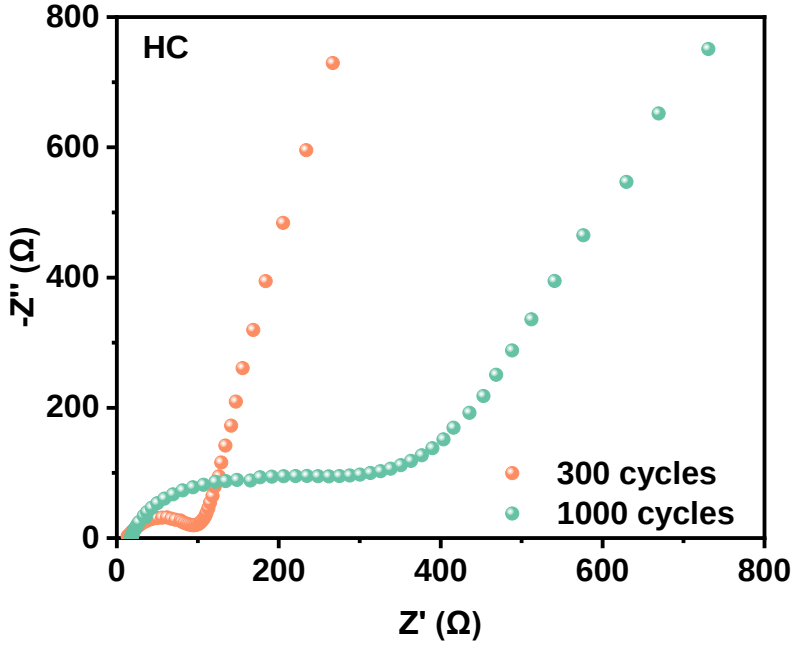

Fig. S43 EIS results of Na||HC half cells (the HC electrodes were from HC||NFM pouch cells cycling at 4.0 V upper voltage).

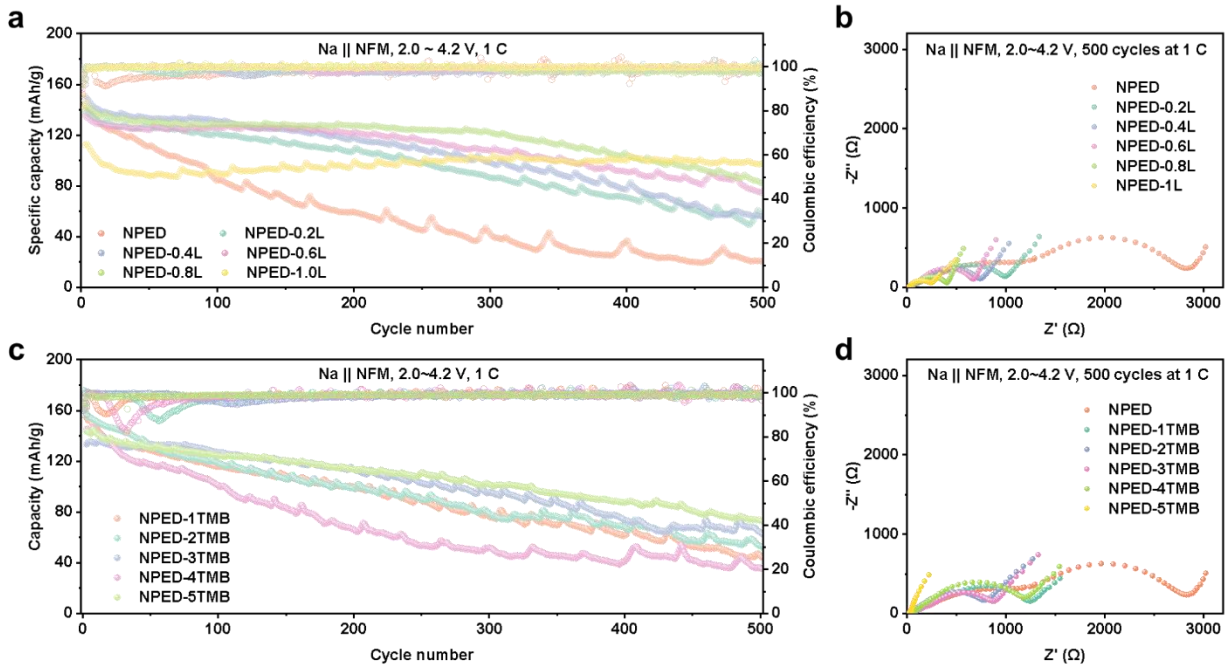

Fig. S44 (a) Cycling performance and (b) EIS after 500 cycles of NFM in electrolytes with a series of LiDFOB with concentration gradients. (c) Cycling performance and (d) EIS after 500 cycles of NFM in electrolytes with a series of TMB with concentration gradients.

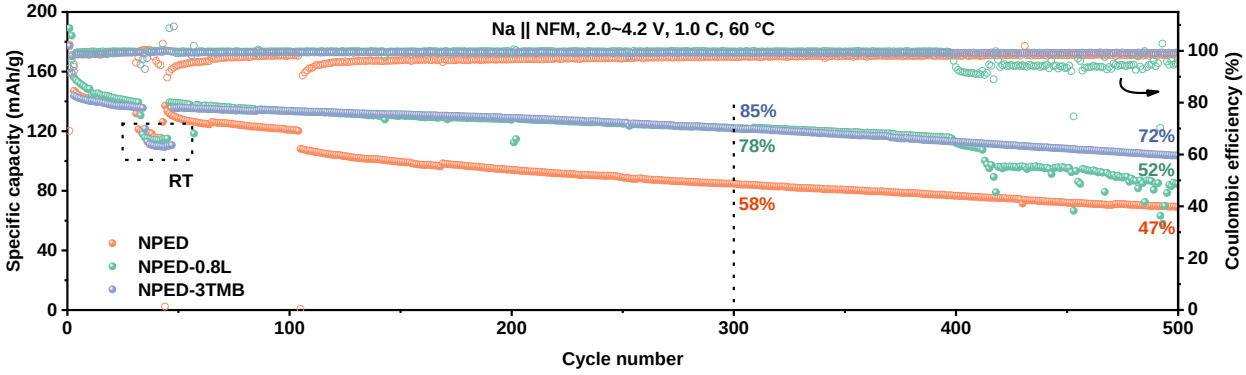

Fig. S45 High-temperature cycling performance of NFM in NPED, NPED-0.8L and NPED-3TMB electrolytes at 4.2 V upper voltage (60 °C).

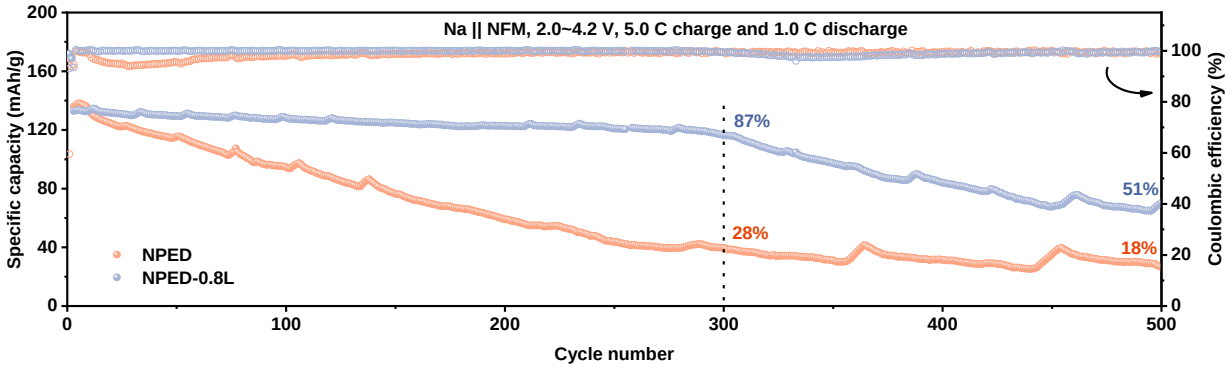

Fig. S46 Fast-charge cycling of NFM in NPED and NPED-0.8L electrolytes at 4.2 V upper voltage (5.0 C current rate).

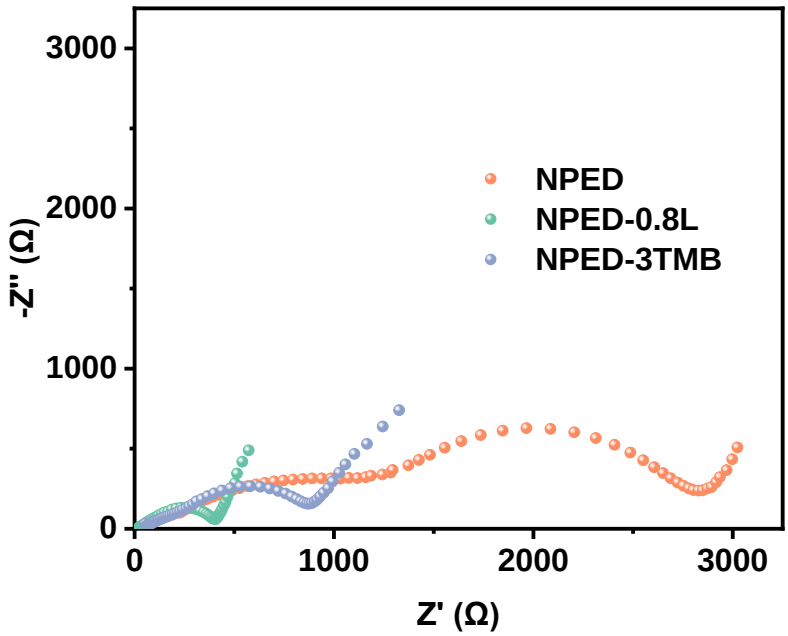

Fig. S47 EIS results of Na||NFM after 500 cycles at 4.2 V upper voltage in NPED, NPED-0.8L and NPED-3TMB electrolytes.

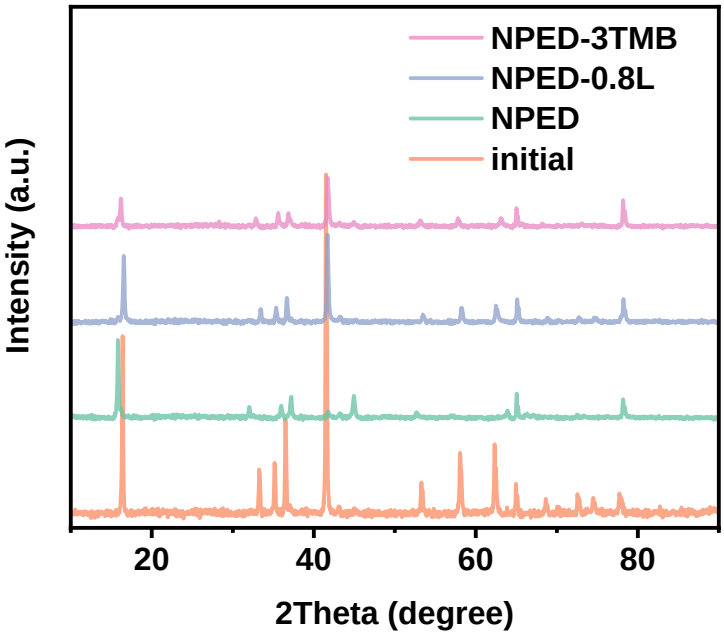

Fig. S48 XRD patterns of NFM, pristine and after 500 cycles at 4.2 V upper voltage in NPED, NPED-0.8L and NPED-3TMB electrolytes.

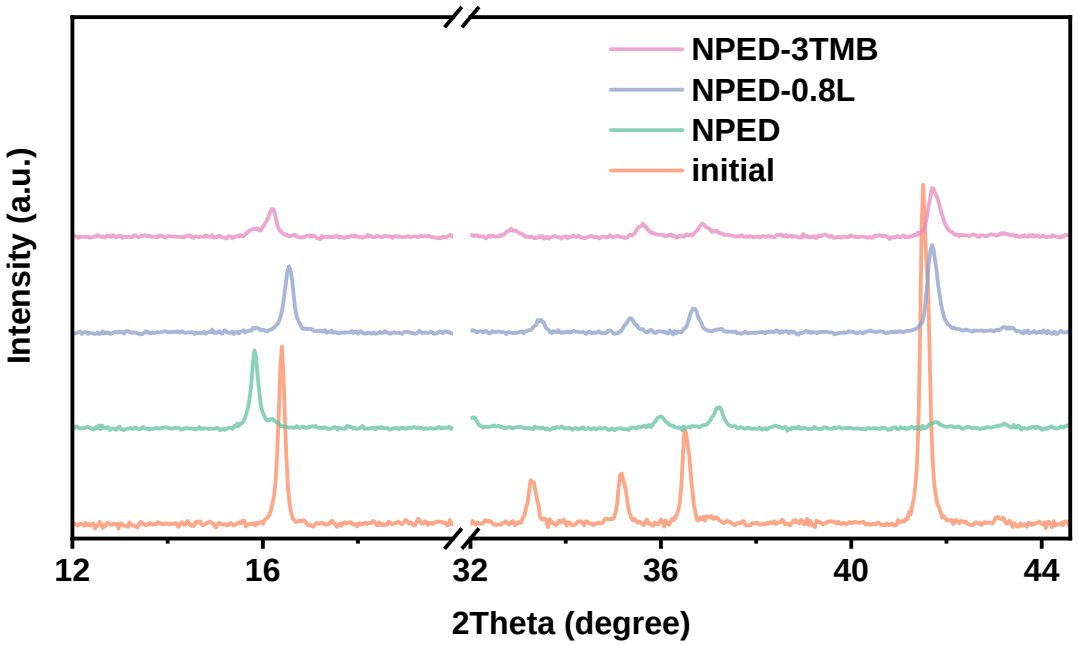

Fig. S49 Local XRD patterns of Fig. S49.

Table S1 Full-cell design parameters.

	cathode	anode
active materials	NFM	HC
mass ratio	96%	95.5%
conductive agent	C (Super P)	C (Super P)
binder	PVDF	CMC, SBR
solvent	NMP	deionized water
theoretical capacity (mAh/g)	130	300
active areal density (mg/cm^2)	15.3	6.9
rolled thickness (um)	120	154
Al foil thickness (um)	12	12
PE separator with 16-um thickness, $NaPF_6$ in EC/PC/DEC with FEC electrolyte, N/P ratio=1.04 (areal capacity of HC to NFM)		

Table S2 (003) peak evolution during cycling of 3.8 V, 4.0 V and 4.2 V.

charging cut-off voltage	state	(003) peak shift versus initial	$d_{(003)}$ (nm)
3.8 V	initial	0	0.550
	fully charged	-0.24°	0.576
	fully discharged	0.03°	0.550
4.0 V	initial	0	0.548
	fully charged	-0.25°	0.568
	fully discharged	-0.03°	0.546
4.2 V	initial	0	0.546
	fully charged	0.32°	0.522
	fully discharged	0.07°	0.540

Table S3 Fitted impedances from Nyquist plots at different charging cut-off voltages during cycling.

charging cut-off voltage	cycle number	Rs (Ω)	R_{CEI} (Ω)	Rct (Ω)
3.8 V	50	5.285	46.48	68.41
	100	14.5	32.21	118.4
	200	8.145	51.71	158.3
	300	5.351	54.67	214.7
4.0 V	50	8.154	25.96	168.4
	100	12.66	31.64	330.2
	200	6.536	37.67	361.6
	300	5.536	53.49	470
4.2 V	50	4.041	19.54	795.9
	100	11.89	28.4	1281
	200	8.231	32.41	1677
	300	13.96	50.03	1754

Reference

1. M. Jeong, *Journal of Power Sources*.
2. J. Liu, Y. You, L. Huang, Q. Zheng, Z. Sun, K. Fang, L. Sha, M. Liu, X. Zhan, J. Zhao, Y.-C. Han, Q. Zhang, Y. Chen, S. Wu and L. Zhang, *Advanced Materials*, 2024, **36**, 2407369.
3. S. Qiu, L. Xiao, M. L. Sushko, K. S. Han, Y. Shao, M. Yan, X. Liang, L. Mai, J. Feng, Y. Cao, X. Ai, H. Yang and J. Liu, *Advanced Energy Materials*, 2017, **7**, 1700403.
4. S. Stankovich, D. A. Dikin, R. D. Piner, K. A. Kohlhaas, A. Kleinhammes, Y. Jia, Y. Wu, S. T. Nguyen and R. S. Ruoff, *Carbon*, 2007, **45**, 1558–1565.